

Thermal wind from hot accretion flows at large radii

De-Fu Bu^{1*} and Xiao-Hong Yang^{2†}

¹Key Laboratory for Research in Galaxies and Cosmology, Shanghai Astronomical Observatory, Chinese Academy of Sciences, 80 Nandan Road, Shanghai 200030, China

²Department of Physics, Chongqing University, Chongqing 400044, China

12 August 2018

ABSTRACT

We study slowly rotating accretion flow at parsec and sub-parsec scale irradiated by a low luminosity active galactic nuclei. We take into account the Compton heating, photoionization heating by the central X-rays. The bremsstrahlung cooling, recombination and line cooling are also included. We find that due to the Compton heating, wind can be thermally driven. The power of wind is in the range $(10^{-6} - 10^{-3})L_{\text{Edd}}$, with L_{Edd} being the Eddington luminosity. The mass flux of wind is in the range $(0.01 - 1)\dot{M}_{\text{Edd}}$ ($\dot{M}_{\text{Edd}} = L_{\text{Edd}}/0.1c^2$ is the Eddington accretion rate, c is speed of light). We define the wind generation efficiency as $\epsilon = P_W/\dot{M}_{\text{BH}}c^2$, with P_W being wind power, \dot{M}_{BH} being the mass accretion rate onto the black hole. ϵ lies in the range $10^{-4} - 1.18$. Wind production efficiency decreases with increasing mass accretion rate. The possible role of the thermally driven wind in the active galactic feedback is briefly discussed.

Key words: accretion, accretion discs – black hole physics – hydrodynamics.

1 INTRODUCTION

Hot accretion flow is believed to operate in low-luminosity active galactic nuclei (LLAGNs; e.g. Ho 2008; Antonucci 2012; Done 2014) and the hard/quiescent states of black hole X-ray binaries (e.g. Esin et al. 1997; Fender et al. 2004; Zdziarski & Gierliński 2004; Remillard & McClintock 2006; Narayan & McClintock 2008; Bolloni 2010; Wu et al. 2013; Yuan & Narayan 2014). Hot accretion flow was studied analytically in the 1990s (Narayan & Yi 1994, 1995; Abramowicz et al. 1995; Kato et al. 1998, Narayan et al. 1998). Later on, numerical simulations have been performed to study the properties of hot accretion flow (e.g. Stone et al. 1999; Igumenshchev & Abramowicz 1999; 2000; Hawley et al. 2001; Machida et al. 2001; De Villiers et al. 2003; Pen et al. 2003; Beckwith et al. 2008; Pang et al. 2011; Tchekhovskoy et al. 2011; McKinney et al. 2012; Yuan et al. 2012a; 2012b; Sądowski et al. 2013; Mościbrodzka et al. 2014).

One of the most important results found by numerical simulations is that strong wind exists in hot accretion flow (e.g. Yuan et al. 2012b; Yuan et al. 2015; Narayan et al. 2012; Li et al. 2013; see also Moller & Sądowski 2015). Recently, observations of both LLAGNs (e.g. Crenshaw & Krammer 2012; Tombesi et al. 2010; 2014; Wang et al. 2013; Cheung et al. 2016) and the hard state of black hole X-ray binaries (Homan et al. 2016) show that winds are present in hot

accretion flow. Therefore, the numerical simulation result is confirmed by observations.

The studies mentioned above focus on the flow at the region very close to the black hole. The outer boundary of the simulations is several hundreds of r_s (r_s is Schwarzschild radius). Then a question is that what are the properties of accretion flow beyond hundreds of r_s ? Can the result from the above mentioned simulations be applied to the accretion flow at sub-parsec and parsec scale? The sub-parsec and parsec scale accretion flow connects the flow in the AGNs and the flow beyond the Bondi radius. The feeding gas of the central black hole comes from this region. Therefore, it is important to study the properties of accretion flow at sub-parsec and parsec scales.

Recently, Li et al. (2013) and Inayoshi et al. (2017) study the accretion flow at parsec and sub-parsec scales. They find that if the gas density is low enough and radiation is not important, the properties of the flow at parsec and sub-parsec scale are similar to the flow inside hundreds of r_s . We note that in these two works, the AGNs feedback is not taken into account. However, AGNs feedback effects (e.g. momentum feedback and energy feedback) are very important to determine the properties of the flow at parsec scale (e.g. Magorrian et al. 1998; Ferrarese & Merritt 2000; Gebhardt et al. 2000; Di Matteo et al. 2005; Ciotti & Ostriker 2007; Kormendy & Bender 2009; Ostriker et al. 2010; Yuan & Li 2011; Liu et al. 2013; Gan et al. 2014) and need to be taken into account.

Recently, the accretion flow at sub-parsec and parsec

* E-mail: dfbu@shao.ac.cn (DB)

† E-mail: yangxh@cqu.edu.cn

scale irradiated by a quasar is studied (e.g. Proga 2007; Kurosawa & Proga 2009). It is found that outflows at parsec-scale can be driven by line force due to interaction of UV photons and the not fully ionized gas.

In this paper, we focus on the accretion flow at sub-parsec and parsec scale irradiated by a LLAGN. Different from a quasar, LLAGNs emit the majority of photons in X-ray band (Yuan & Narayan 2014). The X-ray from the vicinity of black hole can heat the gas at sub-parsec and parsec scale. If the radiation is strong enough, the temperature of the gas at parsec scale will be heated to be above the virial temperature, so that the accretion process will be stopped. In this paper, in addition to the Compton heating/cooling, we also consider the photoionization heating/recombination cooling, bremsstrahlung cooling and line cooling. In this paper, as a first step, we consider gas with small angular momentum.

The paper is organized as follows. In section 2, we describe our models and method; In section 3, we present our results; Section 4 is devoted to conclusions and discussions.

2 NUMERICAL METHOD AND MODELS

In this paper, we study the accretion flow at sub-parsec and parsec scales. We define LLAGN to be the accretion flow inside the inner boundary of our simulation which is not resolved. We assume that all the photons emitted by the central LLAGN are in X-ray band. The luminosity of the LLAGN is self-consistently determined based on the mass accretion rate through the inner boundary. We set that the inner boundary of the computation domain is much larger than the radius ($20r_s$) inside which most of the radiation is produced by the LLAGN. Therefore, the radiation of LLAGN can be approximated to be from a point object located at $r = 0$ and be isotropic.

In this work, we take $2\%L_{\text{Edd}}$ to be the upper limit of the luminosity of the central LLAGN. Above $2\%L_{\text{Edd}}$, the spectrum of a black hole may transit from hard to soft state (e.g. Yuan & li 2011). We only consider the cases in which the luminosity of central LLAGN is below $2\%L_{\text{Edd}}$.

2.1 Basic equations

We assume the accretion flow to be axisymmetric. We use the ZEUS-MP code (Hayes et al. 2006) in spherical coordinates (r, θ, ϕ) to solve the HD equations below:

$$\frac{d\rho}{dt} + \rho \nabla \cdot \mathbf{v} = 0, \quad (1)$$

$$\rho \frac{d\mathbf{v}}{dt} = -\nabla p - \rho \nabla \Phi \quad (2)$$

$$\rho \frac{d(e/\rho)}{dt} = -p \nabla \cdot \mathbf{v} + \dot{E} \quad (3)$$

Here, ρ is the mass density, \mathbf{v} is the velocity, p is gas pressure, e is internal energy. We adopt an equation of state of ideal gas $p = (\gamma - 1)e$ with adiabatic index $\gamma = 5/3$. $\Phi = -GM/(r - r_s)$ is the gravitational potential, where

M and G are the central black hole mass and the gravitational constant, respectively. The Schwarzschild radius $r_s = 2GM/c^2$.

Because the luminosity of the central LLAGN is below $2\%L_{\text{Edd}}$, the radiation pressure due to Compton scattering is not important. Therefore, we do not take into account the radiation pressure force in the momentum Equation (2).

In Equation (3), \dot{E} is the net gas energy change rate due to heating and cooling. We consider Compton heating/cooling, bremsstrahlung cooling, photoionization heating, and line and recombination cooling (Sazonov et al. 2005).

$$\dot{E} = n^2(S_C + S_{br} + S_{ph,rec,l}) \quad (4)$$

In this equation, n is gas number density. The Compton heating/cooling is:

$$S_C = 4.1 \times 10^{-35}(T_X - T)\xi \quad (5)$$

In Equation (5), T is gas temperature. T_X is the radiation temperature determined by the spectrum of radiation from the central source. For a quasar, $T_X = 1.9 \times 10^7$ K (Sazonov et al. (2005)). For a LLAGN, T_X will be much higher (Yuan et al. 2009; Xie et al. 2017). Here, we set $T_X = 10^8$ and 10^9 K for the comparison of effect of Compton temperature on results. ξ is the photoionization parameter defined by

$$\xi \equiv \frac{L}{nr^2}e^{-\tau_x}, \quad (6)$$

where $\tau_x (= \int_0^r \rho \kappa_x dr$, where κ_x is the X-ray opacity) is the X-ray scattering optical depth in the radial direction, r is the distance from the central source, the number density of local gas $n = \rho/(\mu m_p)$, μ is the mean molecular weight. We set $\mu = 1$ and $\kappa_x = 0.4 \text{cm}^2 \text{g}^{-1}$ because Thomson scattering dominates the attenuation. The bremsstrahlung cooling can be expressed as

$$S_{br} = -3.8 \times 10^{-27} \sqrt{T} \quad (7)$$

We do not show the exact formula of the sum of photoionization heating, line and recombination cooling. The reason is as follows. Sazonov et al. (2005) shows that when $T > 10^7$ K, $S_{ph,rec,l} \ll S_C, S_{br}$. In this paper, we find that the gas temperature is always comparable to or higher than 10^7 K. Therefore, the dominant heating and cooling processes are Compton heating and bremsstrahlung cooling. For the formula of $S_{ph,rec,l}$, we refer to Equation (A35) of Sazonov et al. (2005).

In reality, the emitted photons by the accretion flow can interact with the accretion flow and change the properties of the flow. In this paper, we do not consider the secondary heating/cooling by the radiation emitted by the gas.

2.2 Luminosity of the central LLAGNs

Luminosity of the central LLAGN is determined by the accretion rate onto the black hole and radiative efficiency. The radiative efficiency depends on the accretion rate and the parameter δ which describes the fraction of the direct viscous heating to electrons.

We define the ‘circularization’ radius (r_{cir}) to be the radius at which the Keplerian angular momentum is equal to the specific angular momentum of the accretion gas. We study low angular momentum accretion flow by setting r_{cir}

to be smaller than the inner boundary of the computational domain. It means that the angular momentum of gas is much smaller than the Keplerian angular momentum of the computational domain. In this case, the shear of rotational velocity in radial direction is negligibly small. Viscosity is proportional to shear of rotational velocity (see Stone, Pringle & Begelman 1999). Therefore, viscosity is also negligibly small. The negligibly small viscosity can not re-distribute angular momentum of gas. Therefore, when the gas falls from large to small radii, the angular momentum is conserved and does not depend on radius. In previous work (Bu et al. 2013), we find that outside of r_{cir} , there is no outflow and the accretion rate is a constant with radius. Thus, we assume that the mass accretion rate is constant with radius between the inner boundary of the computational domain and r_{cir} . Gas can fall onto the black hole from r_{cir} in the presence of viscosity. Previous works show that the mass inflow rate of hot accretion flow with large angular momentum can be described as $\dot{M}_{\text{in}} \propto r^s$, where $s \approx 0$ for $r \lesssim 10r_s$ and $s \approx 0.5$ for $10r_s < r < r_{\text{cir}}$ (Yuan et al. 2012, 2015; Bu et al. 2013, 2016a, 2016b). The accretion rate of the central black hole is calculated as,

$$\dot{M}_{\text{BH}} = \dot{M}_{\text{in}} \left(\frac{10r_s}{r_{\text{cir}}} \right)^{0.5}, \quad (8)$$

In equation (8), \dot{M}_{in} is the mass inflow rate at the inner boundary of computational domain. According to equation (8), the mass inflow rate is constant with radius between r_{cir} and the inner boundary of simulation domain. From r_{cir} to $10r_s$, the mass inflow rate decreases inwards. From $10r_s$ to the black hole horizon, mass inflow rate is constant with radius. After gas falls into the inner boundary of the simulation, one portion of gas will be accreted to the black hole, the other portion of gas will form wind and move outward to larger radii. Therefore, density of gas between black hole and the inner boundary of simulation does not keep increasing with time. In this paper, as a first step, we neglect the mechanical feedback effects by wind generated between $10r_s$ and r_{cir} . The radiative efficiency calculated by Xie & Yuan (2012) in the case of viscous parameter $\alpha = 0.1$ can be described as follows,

$$\epsilon(\dot{M}_{\text{BH}}) = \epsilon_0 \left(\frac{100\dot{M}_{\text{BH}}}{\dot{M}_{\text{Edd}}} \right)^a, \quad (9)$$

where ϵ_0 and a are given in Table 1 of Xie & Yuan (2012) for different δ . We choose the case of $\delta = 0.5$ and have

$$(\epsilon_0, a) = \begin{cases} (1.58, 0.65) & \text{if } \frac{\dot{M}_{\text{BH}}}{\dot{M}_{\text{Edd}}} \lesssim 2.9 \times 10^{-5}; \\ (0.055, 0.076) & \text{if } 2.9 \times 10^{-5} < \frac{\dot{M}_{\text{BH}}}{\dot{M}_{\text{Edd}}} \lesssim 3.3 \times 10^{-3}; \\ (0.17, 1.12) & \text{if } 3.3 \times 10^{-3} < \frac{\dot{M}_{\text{BH}}}{\dot{M}_{\text{Edd}}} \lesssim 5.3 \times 10^{-3}. \end{cases} \quad (10)$$

When $\frac{\dot{M}_{\text{BH}}}{\dot{M}_{\text{Edd}}} > 5.3 \times 10^{-3}$, the radiative efficiency $\epsilon(\dot{M}_{\text{BH}})$ is simply set to be 0.1.

Time is needed for gas moving from the inner boundary of computation domain to black hole. We need to consider the time lag between X-ray photons generation close to the black hole and the accretion rate calculated at the inner boundary of the computational domain (Kurosawa & Proga 2009). Accretion luminosity at a given time is calculated by $L(t) = \epsilon \dot{M}_{\text{BH}}(t - \delta t) c^2$. $\dot{M}_{\text{BH}}(t - \delta t)$ is the net mass accretion rate calculated at time $t - \delta t$. δt is the lag time and equaling to the accretion timescale from the inner boundary of

the simulation domain to the black hole horizon. As introduced above, gas can freely fall from the inner boundary to r_{cir} . Therefore, the time needed for gas traveling from inner boundary of simulation to r_{cir} is $\delta t_1 = r_{\text{in}}/V1$, $V1$ is free fall velocity at r_{in} . The time needed for gas traveling from r_{cir} to $10r_s$ is the viscous timescale at r_{cir} and is calculated by $\delta t_2 = r_{\text{cir}}/V2/\alpha$. $V2$ is free fall velocity at r_{cir} , α is viscous coefficient. The time needed for gas traveling from $10r_s$ to black hole is $\delta t_3 = 10r_s/V3$, $V3$ is free fall velocity at $10r_s$. The total time delay $\delta t = \delta t_1 + \delta t_2 + \delta t_3$. The delay time δt is calculated based on physical considerations. In order to test the effects of changing value of δt , we have carried out model 1aLDT. In model 1aLDT, we set the delay time is 10 times that in model 1a. We find that with the increase of δt , the wind episode becomes slightly shorter and wind becomes slightly violent. The result of model 1aLDT is presented in Table 1.

We assume the black hole is located at $r = 0$. The mass of the black hole is set to be $M = 10^8 M_{\odot}$ (M_{\odot} is solar mass). The computational domain covers a range $500r_s \leq r \leq 10^6 r_s$ (5×10^{-3} parsec $\leq r \leq 10$ parsec) in radial direction and $0 \leq \theta \leq \pi/2$ in θ direction. The radial grids are logarithmically spaced ($dr_{i+1}/dr_i = 1.05$). In θ direction, the grids are uniformly spaced. The resolution in this paper is 140×88 . Axis-of-symmetry and reflecting boundary conditions are applied at the pole (i.e. $\theta = 0$) and the equatorial plane (i.e. $\theta = \pi/2$), respectively. The outflow boundary condition is adopted at the inner radial boundary. At the outer radial boundary (r_{out}), all HD variables except the radial velocity are set to be equal to the initially chosen values when $v_r(r_{\text{out}}, \theta) < 0$ (inflowing); all HD variables in the ghost zones are set to the values at r_{out} , when $v_r(r_{\text{out}}, \theta) > 0$ (outflowing).

We assume the initial density and temperature of the accretion gas are uniform with $\rho = \rho_0$ and $T = T_0$. We also assume that initially $v_r = v_{\theta} = 0$. The angular momentum of the initial condition is set to be $l(\theta) = l_0(1 - |\cos(\theta)|)$, where l_0 equals to the Keplerian angular momentum at the equatorial plane at r_{cir} .

3 RESULTS

We summarize all the models with different parameters in Table 1. We examine the effects of changing density (ρ_0) and temperature (T_0) at the outer boundary. We also examine the effects of changing the radiation temperature T_X . Virial temperature at the outer boundary equals $\sim 10^7$ K. We consider temperature at the boundary is higher than $T_0 = 10^7$ K. Therefore, Bondi radius is located within the computational domain and much less than the outer boundary.

We take model 1a as our fiducial model. In this model, we set $\rho_0 = 10^{-22} \text{g} \cdot \text{cm}^{-3}$ and $T_0 = 2 \times 10^7$ K. According to the temperature, the Bondi radius in this model is located at $1.6 \times 10^5 r_s$. The Compton radius, i.e., the radius at which the local isothermal sound speed (at the Compton temperature, T_X) is equal to the escape velocity, is defined as

$$R_c = \frac{GM\mu m_{\text{H}}}{kT_X} \quad (11)$$

where $\mu = 1$. Given that $T_X = 10^8$ K, we have $R_c = 9 \times 10^4 r_s$. We run the simulation from $t = 0$ to $t = 1.15 \times 10^6$

Table 1. Simulation parameters

Model	T_X (10^8K)	ρ_0 (10^{-22}g cm^{-3})	T_0 (10^7K)	τ_x (at R_c)	$\dot{M}_{\text{in}}(r_{\text{in}})$ ($L_{\text{Edd}}/0.1c^2$)	\dot{M}_{BH} ($L_{\text{Edd}}/0.1c^2$)	$\dot{M}_w(r_{\text{out}})$ ($L_{\text{Edd}}/0.1c^2$)	$P_W(r_{\text{out}})$ (L_{Edd})	$\epsilon(r_{\text{out}})$
(1)	(2)	(3)	(4)	(5)	(6)	(7)	(8)	(9)	(10)
1a	1	1	2	0.015	10^{-2}	1.7×10^{-3}	6.5×10^{-2}	1.7×10^{-6}	10^{-4}
1aLDT	1	1	2	0.019	1.3×10^{-2}	2.2×10^{-3}	9.1×10^{-2}	2.55×10^{-6}	1.16×10^{-4}
2a	1	1	4	0.013	7×10^{-4}	1.2×10^{-4}	2×10^{-1}	1.5×10^{-5}	1.25×10^{-2}
3a	1	1	6	6×10^{-4}	2×10^{-5}	3.4×10^{-6}	1.1×10^{-1}	1.7×10^{-5}	0.5
4a	1	1	10	2.5×10^{-4}	10^{-5}	1.7×10^{-6}	1×10^{-1}	2.2×10^{-5}	1.18
2ad	1	3	4	0.025	3×10^{-2}	5.1×10^{-3}	6×10^{-1}	4×10^{-5}	8×10^{-4}
3ad	1	3	6	0.018	1.2×10^{-2}	2×10^{-3}	8×10^{-1}	8×10^{-5}	4×10^{-3}
4ad	1	3	10	0.021	1.7×10^{-3}	2.9×10^{-4}	9.2×10^{-1}	1.8×10^{-4}	6.2×10^{-2}
1aTx	10	1	2	0.01	1.2×10^{-3}	2×10^{-4}	1.5×10^{-1}	5.5×10^{-6}	2.8×10^{-3}
2aTx	10	1	4	0.009	3.6×10^{-4}	6.1×10^{-5}	2×10^{-1}	1.6×10^{-5}	2.6×10^{-2}
3aTx	10	1	6	2×10^{-4}	2.2×10^{-5}	3.7×10^{-6}	1.1×10^{-1}	1.4×10^{-5}	0.38

Note: Col. 1: model names. Col.2: the Compton temperature of X-ray radiation from central AGNs powered by a hot accretion flow. Cols 3, 4: the density and temperature at the outer boundary, respectively. Col 5: X-ray optical depth measured at the Compton radius.

The optical depth is obtained by integration from inner boundary of simulation to Compton radius. Col. 6: the mass accretion rate measured at the inner boundary of the simulation domain. Col. 7: the mass accretion rate onto the central black hole (see Equation (8) for reference). Col. 8: the mass flux of wind measured at the outer boundary. Col. 9: the power carried by wind measured at the outer boundary (see Equation (17) for definition). Col. 10: the production efficiency of wind (see Equation (18) for definition). Note that the results listed in Cols 5-10 are obtained by time average the data from $t = 1.5 \times 10^5$ to 10^6 year.

year. We find that wind is generated episodically. The logic is as follows. When the gas accretes to the black hole, X-ray photons will be generated and the accretion flow will be heated by the X-ray irradiation. When the gas temperature is increased to be above the Virial value, wind will be formed. Wind takes away the fueling gas of the black hole, accretion rate onto the black hole will be suppressed. Then, the X-ray generation by the central LLAGN is suppressed. The gas at sub-parsec and parsec scale will cool down when the X-ray heating is suppressed and fuel to the central black hole again. Then the wind can be generated again by the X-ray heating of the infalling gas.

Figure 1 shows snapshot of properties of accretion flow (for model 1a) at $t = 6 \times 10^5$ year when wind is present. Wind forms in the region beyond the Compton and Bondi radius $r > 4 \times 10^5 r_s$. In literatures, the widely studied wind driven mechanisms include radiation pressure (e.g., Murray et al. 1995; Murray & Chiang 1997; Proga 2007), magnetic driven (e.g., Blandford & Payne 1982; Emmering et al. 1992; Romanova et al. 1997; Bottorff et al. 2000; Cao 2011; Li & Begelman 2014), and thermal driven (e.g., Begelman et al. 1983; Chelouche & Netzer 2005). In this paper, the accretion flow is irradiated by a hot accretion flow with low mass accretion rate; Therefore, the radiation pressure due to Thomson scattering is not important. The only mechanism for driving wind here is thermally driven. The right panel of Figure 1 shows the ratio between the thermal energy to the gravitational energy of the flow. It is clear that the wind thermal energy is bigger than the gravitational energy. The wind is thermally driven. We note that because the thermal energy of wind is bigger than its gravitational energy, the Bernoulli parameter (defined as the sum of gravitational energy, thermal energy and kinetic energy) of wind is positive. Wind can escape to infinity.

There are also some papers studying wind from a thin disk irradiated by X-ray (e.g., Begelman et al. 1983; Woods et al. 1996; Chelouche & Netzer 2005; Higginbottom et al.

2017; Nomura & Ohsuga 2017). It is found that beyond the Compton radius, wind can be thermally driven above a thin disk.

To quantitatively study the properties of the inflow/outflow component, we calculate the radial dependence of mass inflow, outflow, and net rates as follows: (1) inflow rate

$$\dot{M}_{\text{in}}(r) = 4\pi r^2 \int_{0^\circ}^{90^\circ} \rho \min(v_r, 0) \sin \theta d\theta \quad (12)$$

(2) outflow rate

$$\dot{M}_{\text{out}}(r) = 4\pi r^2 \int_{0^\circ}^{90^\circ} \rho \max(v_r, 0) \sin \theta d\theta \quad (13)$$

and (3) net rate

$$\dot{M}_{\text{net}}(r) = 4\pi r^2 \int_{0^\circ}^{90^\circ} \rho v_r \sin \theta d\theta \quad (14)$$

We also calculate the kinetic and thermal energy carried by the wind as follows:

$$P_k(r) = 2\pi r^2 \int_{0^\circ}^{90^\circ} \rho \max(v_r^3, 0) \sin \theta d\theta \quad (15)$$

$$P_{\text{th}}(r) = 4\pi r^2 \int_{0^\circ}^{90^\circ} e \max(v_r, 0) \sin \theta d\theta \quad (16)$$

The power of wind is defined as:

$$P_W = P_k + P_{\text{th}} \quad (17)$$

Figure 2 shows the radial profiles of time-averaged (from $t = 1.5 \times 10^5$ to 1.15×10^6 year) and angle integrated mass inflow rate (solid line), outflow rate (dashed line) and the net rate (dotted line) in model 1a. The mass fluxes are expressed in unit of the Eddington accretion rate. It is clear the wind becomes important only beyond $3 \times 10^5 r_s$. Beyond this radius, the wind mass flux exceeds the net accretion rate. Inside $3 \times 10^5 r_s$, wind is very weak and almost all of

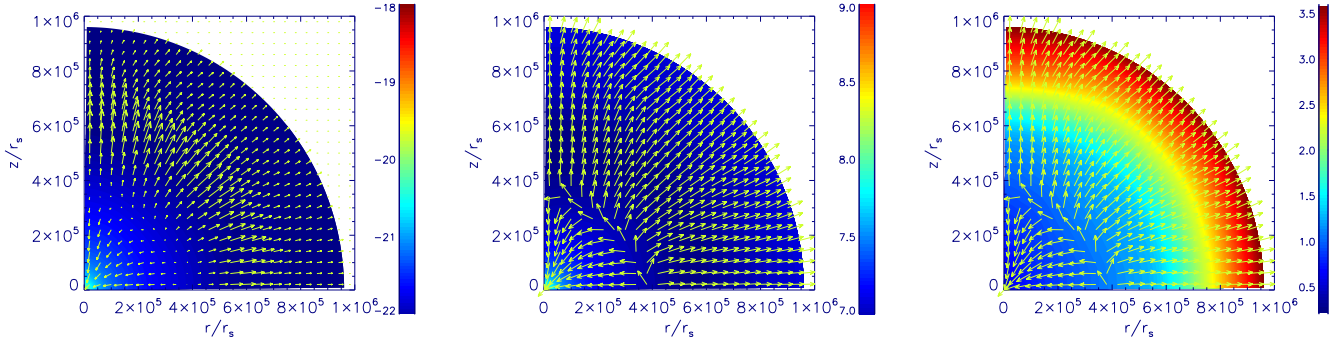


Figure 1. Snapshot of the accretion flow properties at $t = 6 \times 10^5$ year for model 1a. At this snapshot time, the wind is present. Left: logarithm density (colour) overplotted by the poloidal velocity vector (arrows). Middle: logarithm temperature (colour) overplotted by the direction of the velocity vector. Right: the ratio of thermal energy to the gravitational energy. It is clear, in the wind region, the thermal energy is bigger than the gravitational energy.

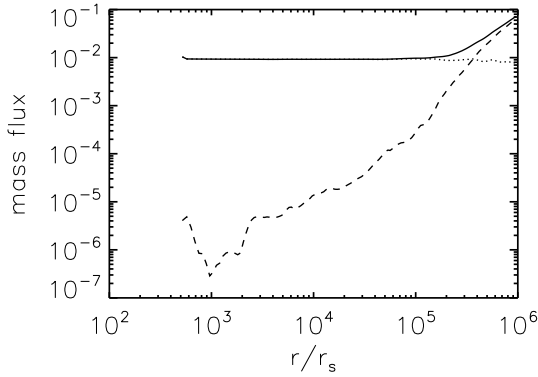


Figure 2. The radial profiles of time-averaged (from $t = 1.5 \times 10^5$ to 1.15×10^6 year) and angle integrated mass inflow rate (solid line), outflow rate (dashed line) and the net rate (dotted line) in model 1a. The mass fluxes are expressed in unit of the Eddington accretion rate.

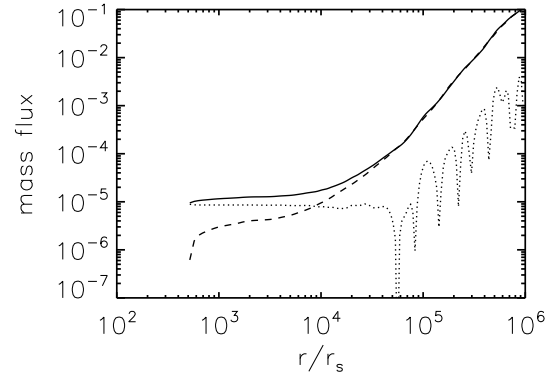


Figure 4. The radial profiles of time-averaged (from $t = 2 \times 10^5$ to 8.5×10^5 year) and angle integrated mass inflow rate (solid line), outflow rate (dashed line) and the net rate (dotted line) in model 4a. The mass fluxes are expressed in unit of the Eddington accretion rate.

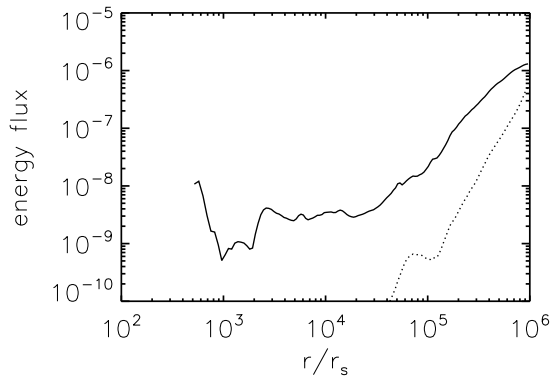


Figure 3. The radial profiles of time-averaged (from $t = 1.5 \times 10^5$ to 1.15×10^6 year) and angle integrated thermal (solid line) and kinetic (dotted line) powers carried by wind in model 1a. The powers are expressed in unit of the Eddington Luminosity.

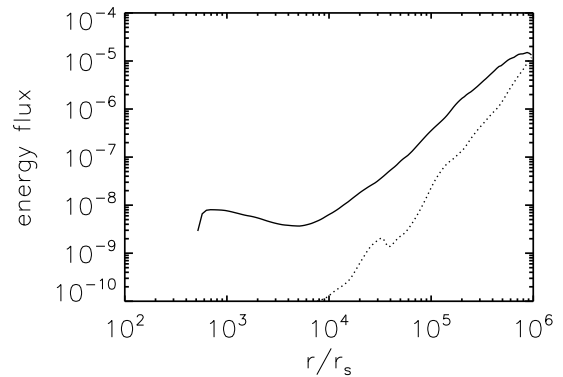


Figure 5. The radial profiles of time-averaged (from $t = 2 \times 10^5$ to 8.5×10^5 year) and angle integrated thermal power (solid line) and kinetic power (dotted line) carried by wind in model 4a. The powers are expressed in unit of the Eddington Luminosity.

the gas falls onto the central black hole. This is consistent with that shown in Figure 1.

Figure 3 shows the radial profiles of time-averaged (from $t = 1.5 \times 10^5$ to 1.15×10^6 year) and angle integrated thermal (solid line) and kinetic (dotted line) powers carried by wind in model 1a. The powers are expressed in unit of the Eddington Luminosity. It is clear that in the whole region, the thermal energy carried by wind is larger than the kinetic energy. It is another evidence that wind is thermally driven. Because wind thermally expands, it can be treated as an expanding ‘atmosphere’, similar to stellar atmospheres. We define the wind production efficiency as

$$\varepsilon = P_w / \dot{M}_{\text{BH}} c^2 \quad (18)$$

\dot{M}_{BH} is calculated by using Equation (8). In model 1a, we find that at the outer boundary $\varepsilon = 10^{-4}$.

We study the effects of changing the outer boundary gas temperature by carrying out models 2a, 3a and 4a. Generally, we find that with the increase of gas temperature, the luminosity of the central AGN decreases. The reason is easy to be understood. With the increase of temperature, the Bondi radius decreases; The mass bound to the black hole is decreased which results in a decrease of mass accretion rate and luminosity.

We take model 4a as an example to illustrate the effects of changing boundary temperature. In model 4a, the outer boundary gas temperature is 5 times of that in model 1a. Figure 4 shows the radial profiles of time-averaged (from $t = 2 \times 10^5$ to 8.5×10^5 year) and angle integrated mass fluxes in model 4a. The mass accretion rate onto the black hole in model 4a is 3 orders of magnitude smaller than that in model 1a. Figure 5 shows the radial profiles of time-averaged (from $t = 2 \times 10^5$ to 8.5×10^5 year) and angle integrated thermal (solid line) and kinetic (dotted line) powers carried by wind in model 4a. Comparing figures 5 and 3, we find that at the outer boundary, the thermal energy flux in model 4a is much higher than that in model 1a. The reason is as follows. Because thermal energy flux is proportional to mass flux of wind times wind temperature. The mass flux of wind at the outer boundary in model 1a is comparable to that in model 4a. However, temperature of wind in model 4a is much higher than that in model 1a. Therefore, wind energy flux in model 4a is higher than that in model 1a. The thermal energy carried by wind in model 4a is larger than kinetic energy. We find that at the outer boundary $\varepsilon = 1.18$ in model 4a.

We study the effects of changing outer boundary density by carrying out models 2ad, 3ad and 4ad. We summarize our results in Table 1. We find that with the increase of density, the mass accretion rate onto the black hole can be significantly increased. The reasons are as follows. As we mentioned above, the temperature of the accretion flow is found to be higher than 10^7 K. The dominating heating and cooling processes are Compton heating and bremsstrahlung cooling. The Compton heating (Equation (5)) is $\propto \rho$, the bremsstrahlung cooling (Equation (7)) is $\propto \rho^2$. With the increase of density, the cooling increases faster than heating. Therefore, the temperature will decrease with increasing density. With the decrease of temperature (or gas pressure gradient force in radial direction), the infall velocity of gas increases. Therefore, with the increase of infall velocity and density, the mass accretion rate onto the black hole

increases. Due to the significant increase of mass accretion rate, the wind production efficiency decreases significantly. We find that when the environment density at pc-scale is higher than $4 \times 10^{-22} \text{ g cm}^{-3}$, the luminosity of the central AGN exceeds $2\% L_{\text{Edd}}$. In this case, the spectrum of black hole has a chance to transit from hard to soft state. We do not discuss this case in which the luminosity of the central AGN exceeds $2\% L_{\text{Edd}}$, because we focus on accretion flow irradiated by a LLAGN.

We take models 3a and 3ad as examples to discuss the effects of changing outer boundary density (see Table 1 for the results). The only difference between models 3a and 3ad is the outer boundary density. The outer boundary density in model 3ad is 3 times higher than that in model 3a. We can see that the mass accretion rate in model 3ad is more than 2 orders of magnitude higher than that in model 3a. The wind mass flux in model 3ad is 8 times of that in model 3a. The increase of wind mass flux is due to the increase of density in the wind region. With the increase of wind mass flux, the power of wind increases. We note that the power of wind is increased by a factor smaller than 8. Because $P_w \propto \dot{M}_w \times T$. Due to the decrease of wind temperature in model 3ad, the increase of wind power is smaller than 8. Due to the high accretion rate in model 3ad, the production efficiency of wind is much smaller than that in model 3a.

We also study the effects of Compton temperature by carrying out models 1aTx, 2aTx and 3aTx. The results are summarized in Table 1. We find that when the temperature of accretion flow is low, the effects of increasing Compton temperature are obvious (see the comparison of results in models 1aTx and 1a presented in table 1). The effects of increasing Compton temperature become less important with the increase of accretion flow temperature (see the comparison of results in models 3aTx and 3a presented in table 1). The reason is as follows. According to equations (4), (5) and (6), the Compton heating in a unit volume is proportional to $L(T_X - T)n$. Therefore, for gas of unit mass, the Compton heating is proportional to $L(T_X - T)$. X-ray luminosity is proportional to mass accretion rate. Therefore, Compton heating is proportional to $\dot{M}(T_X - T)$. Although, the increase of $(T_X - T)$ from model 1a to 1aTx is comparable to the increase of $(T_X - T)$ from model 3a to 3aTx. The mass accretion rates in models 1a and 1aTx are about 2 orders of magnitude higher than those in models 3a and 3aTx (The value of \dot{M} is presented in Table 1). Therefore, the effects of increasing Compton temperature are more obvious in low temperature accretion flow case. We take models 1aTx and 1a as examples to discuss the effects of increasing Compton temperature. We find that accretion rate decreases by a factor of ~ 8 in model 1aTx compared to that in model 1a. The reason is as follows. Higher Compton temperature results in stronger Compton heating and higher gas temperature. When accretion flow temperature becomes higher, the gas infall velocity decreases due to stronger gas pressure gradient force. The accretion rate decreases with decreasing infall velocity. Also, higher temperature can also result in larger wind power, because higher temperature gas has larger specific energy.

In order to summarize the results discussed above, we plot Figure 6. In this figure, diamonds represent results from models 1a-4a. Triangles represent results from models 2ad-4ad. Squares represent results from models 1aTx-3aTx. The

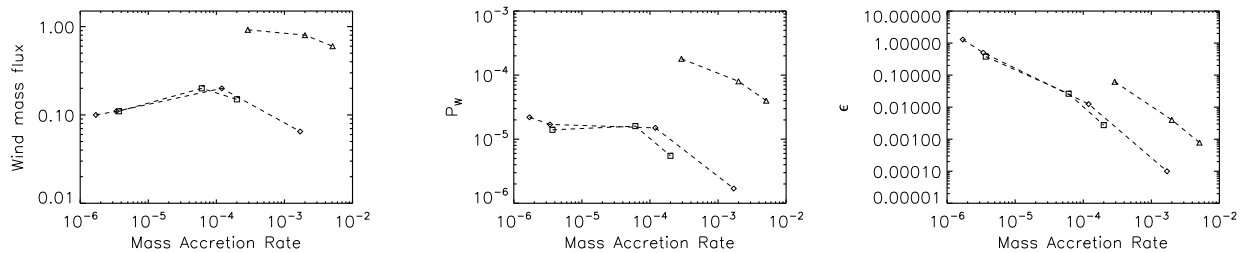


Figure 6. Summary of the results presented in table 1. In this figure, diamonds represent results from models 1a-4a. Triangles represent results from models 2ad-4ad. Squares represent results from models 1aTx-3aTx. The horizontal axis in each panel is accretion rate onto the black hole in unit of Eddington accretion rate. Left: the wind mass flux (in unit of Eddington accretion rate) measured at the outer boundary of the simulation as a function of mass accretion rate. Middle: power of wind (in unit of Eddington luminosity, see Equation (17)) measured at the outer boundary of the simulation as a function of mass accretion rate onto the black hole. Right: wind production efficiency (see Equation (18)) measured at the outer boundary of the simulation as a function of mass accretion rate onto the black hole.

mass flux of wind is in the range $10^{-2} < \dot{M}_W/\dot{M}_{\text{Edd}} < 1$. The power of wind is in the range $10^{-6} < \dot{P}_W/L_{\text{Edd}} < 10^{-3}$. From this figure, we find that the changing of Compton temperature has small effects on results. As introduced above, with the increase of gas density at the outer boundary, the properties of wind change significantly. For example, with the increase of gas density at the outer boundary, wind mass flux and power increase significantly. Correspondingly, the production efficiency of wind increases significantly. Note that the power of wind does not strongly correlate with mass accretion rate, therefore, the wind production efficiency is predominately determined by the black hole accretion rate. Therefore, generally, the production efficiency of wind decreases with increasing mass accretion rate. We note that the production efficiency of wind can be larger than 1, when $\dot{M}_W/\dot{M}_{\text{Edd}} \sim 10^{-6}$. Yuan et al. (2015) studied wind generated in hot accretion flow with larger angular momentum in the region very close to the black hole. They find that wind can be generated by the combination of centrifugal and magnetic pressure gradient forces. In that work, it is found the wind production efficiency is $\sim 1/1000$.

4 SUMMARY AND DISCUSSION

In this paper, we perform two-dimensional hydrodynamical simulations to study slowly rotating accretion flow at parsec and sub-parsec scale irradiated by a LLAGN. We take into account the Compton heating and photoionization heating by the central X-ray. The bremsstrahlung cooling, recombination and line cooling are also taken into account. The temperature of the accretion flow is found to be above 10^7 K. Therefore, the photoionization heating, recombination and line cooling are negligibly small. The dominate heating and cooling processes are Compton heating and bremsstrahlung cooling. We find that due to the Compton heating by the central X-ray, the accretion flow temperature can be above the virial temperature. Wind can be thermally driven. The mass flux of wind is in the range $10^{-2} < \dot{M}_W/\dot{M}_{\text{Edd}} < 1$. The power of wind is in the range $10^{-6} < \dot{P}_W/L_{\text{Edd}} < 10^{-3}$. We find the wind production efficiency decreases with increasing mass accretion rate. The production efficiency of wind is in the range $10^{-4} < \epsilon \leq 1.18$.

In the large scale AGN feedback simulations (e.g., Ciotti

et al. 2010; Gaspari et al. 2012), “mechanical feedback” by AGN wind is usually involved to heat the intercluster medium to prevent rapid cool of the gas (i.e., the cooling flow problem). It is found that to be consistent with observations, the production efficiency should be larger than 10^{-4} . Therefore, the thermally driven wind may play a role in solving the rapid cooling problem of intercluster medium when the AGN is in hot accretion mode.

In this paper, we study slowly rotating accretion flow. In future, it is necessary to study accretion flow with high angular momentum. If the angular momentum of accretion flow is high, a rotating disk can form. Viscosity is needed to transfer angular momentum. There are several big differences between slowly rotating flow and high angular momentum accretion disk, viscous heating can increase the gas temperature; Second, in the high angular momentum accretion flow, gas can fall onto the central black hole on a viscous timescale. Viscous timescale is much longer than the nearly free fall timescale of slowly rotation flow. Therefore, there is a longer time lag between the changing of mass accretion rate at large scale and the response in generation of X-ray photons close to the black hole. Third, in the high angular momentum accretion flow, centrifugal force helps to generate wind.

In accretion flows, ordered, large-scale open magnetic field may exist (e.g. Blandford & Payne 1982; Lovelace et al. 1994; Cao 2011; Penna et al. 2013; Bai & Stone 2013; Li & Begelman 2014). In addition to thermally driven wind, magneto-centrifugal wind may also be present (Blandford & Payne 1982; Cao 2011; Li & Begelman 2014). Therefore, it is necessary to study the accretion flow at parsec scale with magnetic field in future.

ACKNOWLEDGMENTS

We thank the referee for his/her valuable comments which help to improve this paper significantly. This work is supported in part by the National Program on Key Research and Development Project of China (Grant No. 2016YFA0400704), the Natural Science Foundation of China (grants 11573051, 11633006, 11773053 and 11661161012), the Natural Science Foundation of Shanghai

(grant 16ZR1442200), and the Key Research Program of Frontier Sciences of CAS (No. QYZDJSSW-SYS008). This work made use of the High Performance Computing Resource in the Core Facility for Advanced Research Computing at Shanghai Astronomical Observatory.

REFERENCES

- Abramowicz M. A., Chen X., Kato S., Lasota J. P., Regev O., 1995, *ApJL*, 438, L37
- Antonucci R., 2012, *A&AT*, 27, 557
- Bai X. N., Stone J. M., 2013, *ApJ*, 767, 30
- Beckwith K., Hawley J. F., Krolik J. H., 2008, *ApJ*, 678, 1180
- Begelman M. C., McKee C. F., Shields G. A., 1983, *ApJ*, 271, 70
- Belloni T. M., 2010, in Belloni T., ed., *Lecture Notes in Physics*, Vol. 794, *The Jet Paradigm - From Microquasars to Quasars*. Springer-Verlag, Berlin, p. 53
- Blandford R. D., Payne D. G., 1982, *MNRAS*, 199, 883
- Bottorff M. C., Korista K. T., Shlosman I., 2000, *ApJ*, 537, 134
- Bu D. F., Yuan F., Wu M. C., Cuadra J. 2013, *MNRAS*, 434, 1692
- Bu D. F., Yuan F., Gan Z. M., Yang X. H. 2016a, *ApJ*, 818, 83
- Bu D. F., Yuan F., Gan Z. M., Yang X. H. 2016b, *ApJ*, 823, 90
- Cao X. W., 2011, *ApJ*, 737, 94
- Chelouche D., Netzer H. 2005, *ApJ*, 625, 95
- Cheung E., Bundy K., Cappellari M., et al. 2016, *Nature*, 533, 504
- Ciotti L., Ostriker J. P., 2007, *ApJ*, 665, 1038
- Ciotti L., Ostriker J. P., Proga D., 2010, *ApJ*, 717, 708
- Crenshaw D. M., Kraemer S. B., 2012, *ApJ*, 753, 75
- De Villiers J. P., Hawley J. F., Krolik J. H., 2003, *ApJ*, 599, 1238
- Di Matteo T., Springel V., Hernquist L., 2005, *Natur*, 433, 604
- Done C., 2014, in Ishida M., Petre R., Mitsuda K., eds, *Suzaku-MAXI 2014: Expanding the Frontiers of the X-ray Universe*. Ehime University, Matsuyama, Ehime Prefecture, Japan, p. 300
- Esin A. A., McClintock J. E., Narayan R., 1997, *ApJ*, 489, 865
- Emmering R. T., Blandford R. D., Shlosman I., 1992, *ApJ*, 385, 460
- Fender R. P., Belloni T. M., Gallo E., 2004, *MNRAS*, 355, 1105
- Ferrarese L., Merritt D., 2000, *ApJ*, 539, 9
- Gan Z. M., Yuan F., Ostriker J. P., Ciotti L., Novak G. S., 2014, *ApJ*, 789, 150
- Gaspari M., Brighenti F., Temi P., 2012, *MNRAS*, 424, 190
- Gebhardt K., Bender R., Bower G., 2000, *ApJ*, 539, L13
- Hawley J. F., Balbus S. A., Stone J. M., 2001, *ApJ*, 554, L49
- Hayes J. C., Norman M. L., Fiedler R. A., Bordner J. O., Li P. S., 2006, *ApJ*, 165, 188
- Higginbottom N., Proga D., knigge C., Long K. S., 2017, *ApJ*, 836, 42
- Ho L. C., 2008, *ARA&A*, 46, 475
- Homan J., Neilson J., Allen J. L., et al. 2016, *ApJ*, 830, L5
- Inayoshi K., Ostriker J. P., Haiman Z., Kuiper R., 2017 (arXiv: 1709.07452)
- Igumenshchev I. V., Abramowicz M. A., 1999, *MNRAS*, 303, 309
- Igumenshchev I. V., Abramowicz M. A., 2000, *ApJS*, 130, 463
- Kato S., Fukue J., Mineshige S., 1998, *Black Hole Accretion Disks*. Kyoto Univ. Press, Kyoto
- Kormendy J., Bender R., 2009, *ApJ*, 691, L142
- Kurosawa R., Proga D., 2009, *MNRAS*, 397, 1791
- Lovelace R. V. E., Romanova M. M., Newman W. I., 1994, *ApJ*, 437, 136
- Li J., Ostriker J., Sunyaev R., 2013, *ApJ*, 767, 105
- Li S. L., Begelman M. C., 2014, *ApJ*, 786, 6
- Liu C., Yuan F., Ostriker J., Gan Z., Yang X., 2013, *MNRAS*, 434, 1721
- Machida M., Matsumoto R., Mineshige S., 2001, *PASJ*, 53, L1
- Magorrian J., Tremaine S., Richstone D. et al. 1998, *AJ*, 115, 2285
- McKinney J., Tchekhovskoy A., Blandford R., 2012, *MNRAS*, 423, 3083
- Moller A., Sadowski A., 2015 (arXiv:1509.06644)
- Mościbrodzka M., Falcke H., Shiokawa H., Gammie C. F., 2014, *A&A*, 570, A7
- Murray N., Chiang J., Grossman S. A., Voit G. M., 1995, *ApJ*, 451, 498
- Murray N., Chiang J., 1997, *ApJ*, 474, 91
- Narayan R., Yi I., 1994, *ApJ*, 428, L13
- Narayan R., Yi I., 1995, *ApJ*, 452, 710
- Narayan R., Mahadevan R., Quataert E., 1998, in Abramowicz M. A., Bjornsson G., Pringle J. E., eds, *Theory of Black Hole Accretion Discs*. Cambridge Univ. Press, Cambridge, p. 148
- Narayan R., McClintock J. E., 2008, *New Astron. Rev.*, 51, 733
- Narayan R., Sadowski A., Penna R. F., Kulkarni A. K., 2012, *MNRAS*, 426, 3241
- Nomura M., Ohsuga K., 2017, *MNRAS*, 465, 2873
- Ostriker J. P., Choi E., Ciotti L., Novak G. S., Proga D., 2010, *ApJ*, 722, 642
- Pang B., Pen U.-L., Matzner C. D., Green S. R., Lieben-dorfer M., 2011, *MNRAS*, 415, 1228
- Pen U. L., Matzner C. D., Wong S., 2003, *ApJ*, 596, L207
- Penna R. F., Sadowski A., Kulkarni A. K., Narayan R., 2013, *MNRAS*, 428, 2255
- Proga D., 2007, *ApJ*, 661, 693
- Remillard R. A., McClintock J. E., 2006, *ARA&A*, 44, 49
- Romanova M. M., Ustyugova G. V., Koldoba A. V., Chechetkin V. M., Lovelace R. V. E., 1997, *ApJ*, 482, 708
- Sadowski A., Narayan R., Penna R., Zhu Y., 2013, *MNRAS*, 436, 3856
- Sazonov S. Y., Ostriker J. P., Ciotti L., Sunyaev R. A., 2005, *MNRAS*, 358, 168
- Stone J. M., Pringle J. E., Begelman M. C., 1999, *MNRAS*, 310, 1002
- Tchekhovskoy, A., Narayan R., McKinney J. C., 2011, *MNRAS*, 418, L79
- Tombesi F., Sambruna J. N., Reeves J. N., et al. 2010, *ApJ*, 719, 700

- Tombesi F., Tazaki F., Mushotzky R. F., et al. 2014, MNRAS, 443, 2154
- Wang Q. D., Nowak M. A., Markoff S. B., et al., 2013, Sci, 341, 98
- Woods D. T., Klein R. I., Castor J. I., McKee C. F., Bell J. B., 1996, ApJ, 461, 767
- Wu Q. W., Cao X., Ho L. C., Wang D. X., 2013, ApJ, 700, 31
- Xie F., Yuan F., 2012, ApJ, 427, 1580
- Xie F., Yuan F., Ho L. C., 2017, ApJ, 844, 42
- Yuan F., Xie F., Ostriker J. P., 2009, ApJ, 691, 98
- Yuan F., Li M., 2011, ApJ, 737, 23
- Yuan F., Wu M. C., Bu D. F., 2012a, ApJ, 761, 129
- Yuan F., Bu D. F., Wu M. C., 2012b, ApJ, 761, 130
- Yuan F., Narayan R., 2014, ARA&A, 52, 529
- Yuan F., Gan Z. M., Narayan R., Sadowski A., Bu D. F., Bai X. N., 2015, ApJ, 804, 101
- Zdziarski A. A., Gierliński M., 2004, PThPS, 155, 99